IEEE Access
Multidisciplinary | Rapid Review | Open Access Journal

Received 12 April 2023, accepted 26 April 2023, date of publication 1 May 2023, date of current version 10 May 2023.

Digital Object Identifier 10.1109/ACCESS.2023.3271861

RESEARCH ARTICLE

Dynamics Modeling and Autonomous Landing for Flexible Parafoil-Vehicle Multibody System

LUQI YAN, YANGUO SONG, HUANJIN WANG, AND ZHIWEI SHI
College of Aerospace Engineering, Nanjing University of Aeronautics and Astronautics, Nanjing, Jiangsu 210016, China
Corresponding author: Huanjin Wang (whj@nuaa.edu.cn)

This work was supported by the National Natural Science Foundation of China under Grant 11972192.

ABSTRACT In this paper, the autonomous landing of the parafoil used for aerial vehicles is investigated through the numerical approach. The coupled parafoil-vehicle dynamics model is developed based on the multibody method. The transition process from aircraft flight to parafoil glide is designed in a global system framework. To deal with large flexible deformations during the deployment process, the parafoil canopy is approximated as interacting symmetric subparts using the geometric division method. The pseudo-spectral method is employed to generate a reference trajectory for the landing target. As the system dynamics are introduced into constraint conditions, the generated trajectory is beneficial to improve landing precision. In addition, other optimization objectives, including minimal energy consumption and obstacle avoidance, are considered in trajectory planning. The enhanced proportional integral control is designed to follow the reference trajectory. The neural network inversion model is used to reduce the coupling effect between the longitudinal and the directional control channels. There is a coupling effect that the two controls both are implemented through left and right trailing-edge deflections. An adaptive output allocation method is proposed to ensure that the directional control always is effective in particular when one side reaches saturation. Finally, simulations for autonomous landing under different conditions are carried out to validate the integrated system.

INDEX TERMS Flexible parafoil model, multi-body system, trajectory optimization, flight control.

I. INTRODUCTION

Compared with traditional round parachutes, parafoils have better aerodynamic performance and maneuverability that the airflow through the leading-edge cut maintains the shape of the airfoil section, and the trailing-edge deflections can be used to adjust flight direction and implement flared landings. At present, parafoils have been applied to some vehicles for recoveries [1], such as fixed-wing aircraft, reentry vehicles, and rocket parts, and the autonomous landing technology of the parafoil has become a research focus.

The parafoil dynamics model is the research basis of an autonomous control system. There are some dynamics models presented according to the rigid body and the multibody methodologies [2], [3], [4]. For the rigid body model, the parafoil and the payload are considered as a whole, and the relative distance between the canopy and the payload remains constant. The multibody model introduces the specific connection structure, and the relative movements can be obtained and analyzed in this way. Some identification methods were used to obtain aerodynamic coefficients. Wu et al. [5] performed simulations of computational fluid dynamics and estimated the leading-edge cut and the deflection factors utilizing the least-squares method. Zhu et al. [6], [7] calculated the aerodynamic forces based on the database from fluid-structure interaction simulations, and the influences of canopy inflation, trailing-edge deflections, and wind fields were analyzed. Because the payload and the canopy are connected by flexible suspension lines, it is difficult to gather complete flight data through sensors. Ward et al. [8] provided a six-degree-of-freedom (DOF) model in which the aerodynamic coefficient was identified by Global Positioning System data without inertial measurement.

The general dynamics models are only used for steady glide. Although the aerodynamic force on the parafoil can be calculated as the sum of contributions from the divided

The associate editor coordinating the review of this manuscript and approving it for publication was Halil Ersin Soken.

canopy subparts, the canopy still is regarded as a rigid body during the flight even for the multibody model. It is difficult to deal with the complete airdrop process with large flexible deformations, especially in the case of the parafoil-vehicle system involving multiple flight stages. The parafoil model with higher degrees of freedom is needed to develop further. Therefore, we build a detailed model according to the surface division. There is an individual coordinate system for each canopy subpart, and the kinematic equations are built to describe the motion of every subpart. The canopy deformations are presented through the relative movements between the adjacent subparts.

A reasonable guidance trajectory is necessary for the autonomous system to ensure an accurate landing. For the unpowered parafoil, the planned trajectory should first meet the system dynamics to reduce control difficulty. The complex environment, like obstacles and wind disturbances, also brings some challenges to make a precise landing. The environmental factors should be considered in trajectory planning. There have been some common algorithms of path planning, like the dynamic optimization method and the intelligent search method [9]. The rapidly-exploring random tree (RRT) algorithm can be used to obtain a trajectory of avoiding obstacles or resisting winds in a short time [10], [11]. But the trajectories generated through RRT usually are not smooth enough, which brings difficulty in guidance design. Some planning methods integrated with flight dynamics were used to produce continuous and smooth trajectories [12], [13], [14], [15]. Fowler and Rogers [16] designed the guidance path composed of multiple cubic Bézier curves, where the turn rate in each segment is limited within its maximum and the descent rate varies with the current yaw rate instead of being constant. Gorman and Slegers [17] compared parafoil models with six to nine degrees of freedom using experimental data and found that the six DOF model was adequate for the design of the trajectory following. For the external wind disturbance, Rogers and Slegers [18] sorted the possible trajectories produced by parallel Monte Carlo simulation following wind uncertainty, and obtained the pathway suitable for a realistic environment.

There are always position differences from the reference trajectory as a result of external disturbances during flight. To correct directional errors, Prakash and Ananthkrishnan [19] designed a controller using the nonlinear dynamic inversion method and kept longitudinal and lateral loops open given the natural pendulum stability of the parafoil. Other traditional control methods were used for the parafoil [20], [21], [22], including proportional-integral-derivative (PID) control with parameter optimization, model predictive control, etc. Gockel [23] discovered that the deviation from the planned path is mostly caused by the wind prediction error rather than the observation error and delay of the flight state within a certain range. The disturbance rejection technique is able to effectively handle the issues of system uncertainties and external disturbances [24]. Sun et al. [25] designed an improved active disturbance rejection controller to compensate for the constant wind and gusts.

The response speed of the parafoil glide ratio to input is slow and it is not enough effective to control glide slope, therefore the longitudinal channel generally is designed as the open loop system for unpowered parafoils. Ward et al. [26], [27] proposed the adjustable incidence angle and gravity center combined with the trailing-edge deflection to achieve glide ratio control. Besides, the technology of upper-surface canopy spoilers was proven to be an effective method for longitudinal control [28], [29]. But it should be noticed that these auxiliary measures also would increase system complexity and make applications more challenging.

The combination design of trajectory planning and tracking is necessary for autonomous motion control problems to achieve better effects [30]. Especially for the unpowered parafoil system, the landing precision is dependent on the guidance trajectory in addition to flight control. To adapt to different work conditions, trajectory planning with multiple objectives is designed through the pseudo-spectral method in the paper. As the parafoil enters into a turning flight, the glide ratio will appear a reduction. The coupling effect between the directional and the longitudinal channels can bring the degradation of control performance. Considering that the neural network is effective to deal with the nonlinear control problem for multi-input and multi-output systems [31], [32], we utilize the neural network (NN) inversion model trained in various flight conditions to enhance the controller. Meanwhile, the output allocating method is proposed to ameliorate the degradation of direction control induced by the saturation of the trailing-edge deflections.

The main contributions of this paper are summarized as follows:

1) The dynamics model of the parafoil-vehicle system is developed to handle large flexible deformations in the transition from aircraft flight to parafoil glide.
2) The combination of flight control and trajectory planning is employed to improve landing precision under different work conditions.
3) The inversion model is used to achieve direction and glide ratio controls, and an output allocation method is provided to ameliorate the problem of performance loss induced by the control saturation.

The remainder of this paper is organized as follows. In section II, the system framework involving the airdrop process is designed. The multibody dynamics model of the parafoil-vehicle system is built, and the external forces on parafoil and aircraft are calculated, respectively. In section III, the flexible modeling method is compared with the 6 DOF and 9 DOF models. The data of glide ratio obtained from the flight experiment is compared with the model. In section IV, the trajectory planning is designed as an optimization problem based on the pseudo-spectral method, in which the optimal objectives include landing precision,

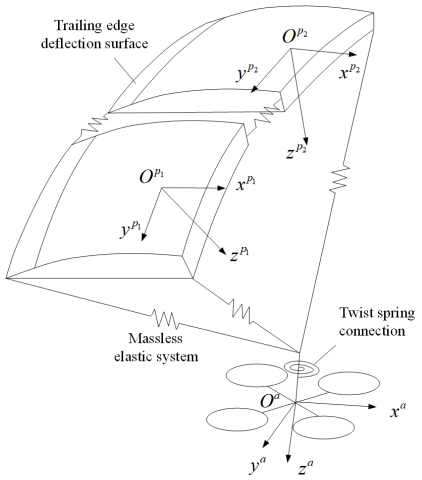

FIGURE 1. The discrete structure of the parafoil-quadrotor coupling system.

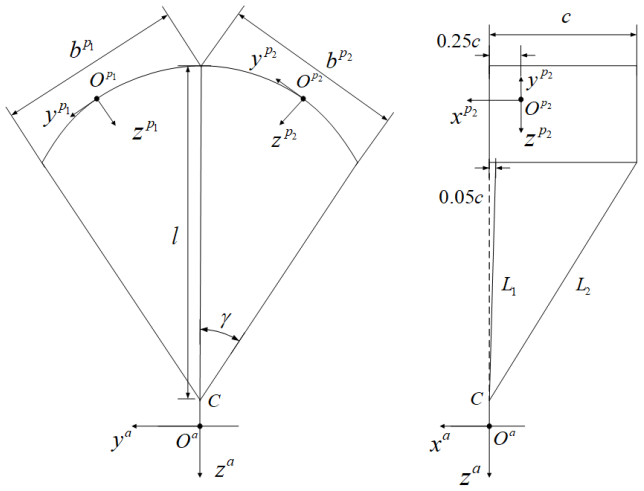

FIGURE 2. The front and side views of the geometric structure of the multibody system.

energy consumption, and obstacle avoidance. The reference trajectory is obtained after the optimization problem is transformed into the discrete form and solved. In section V, the output allocation between directional and longitudinal controls is proposed. Then, the neural network inversion model combined with the proportional integral control is designed. In section VI, simulations under different conditions, including landing precision, wind resistance, and obstacle avoidance, are performed to validate the designed autonomous system.

II. MODELING THE PARAFOIL-VEHICLE DYNAMICS SYSTEM

As illustrated in Fig. 1, the parafoil carried by a quadrotor aircraft is composed of a canopy and several suspension lines. The canopy is separated into two symmetric parts p_i ($i = 1, 2$) connected by inner forces. There are three moving coordinates fixed at the mass centers of the canopy subparts and the aircraft, respectively. The single-point connection between the parafoil and the aircraft is a twist spring system providing a directional restoring moment for the aircraft [33].

A. MODEL FRAMEWORK OF THE PARAFOIL-VEHICLE SYSTEM

The flight performance is influenced by selected parameters, such as aspect ratio and line length [34]. The parafoil structure is designed as shown in Fig. 2. For different requirements of structure configurations, the outside line length L_i and the span b^{p_i} are fixed. The distance l from canopy top to connection point C, and the half angle γ are interrelated that lowering l will result in an increase of γ and a decrease in canopy camber. Suspension lines are attached to the corners of the canopy and their natural lengths are determined by the designed geometry. The mass center for each canopy subpart is assumed to be in the quarter-chord line. The aircraft is located beneath the leading edge of the canopy. Because of the existence of the leading-edge cut, the connection point on the canopy is in the 5% chord line.

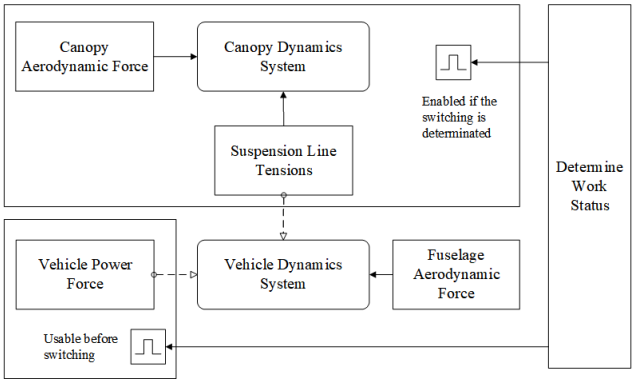

FIGURE 3. The basic model framework of the parafoil-vehicle system.

For the parafoil-vehicle system includes, the flight can be divided into three stages, including the powered flight of the aircraft, the transition phase, and the unpowered glide of the parafoil. The dynamics properties are quite different between these stages. Hence, a global model framework is proposed as shown in Fig. 3. The current system status is determined by a global module. The parafoil is regarded as packed and has no impact on the vehicle during the powered flight. After the parafoil is activated, the aerodynamics and dynamics of the canopy are introduced, and the tensions of suspension lines are calculated and exerted on the aircraft and the canopy. Meanwhile, the rotors of the aircraft stop working and their thrusts disappear.

When the parafoil is dragged out of the container, there are not enough air masses to maintain the aerodynamic profile of the canopy. After the suspension lines are stretched and the canopy is pressurized, the air cells in the center of the canopy are inflated first, followed by the outboard air cells as the internal pressure rises. Because there are few aerodynamic effects during this process, the stretching course of suspension lines is ignored, and the initial state of the parafoil is set at the canopy inflated with a partial aerodynamic area.

The effective aerodynamic area changes throughout the deployment process. For this transition, the mathematical dynamics model is different from the computational fluid dynamics approach that there are no air masses to develop the inflation course in the simulation environment. Thus, the parafoil inflation model proposed by Potvin [35] is employed. During the deployment process, the vertical motion equation of the system is expressed as:

$$mv' = \rho \sum v^2/2 - W \tag{1}$$

where, m is the system mass, v is the vertical speed, ρ is the air density, W is the total weight, and Σ represents the instant drag area of the parafoil. The dynamic change of drag area Σ is approximately given as:

$$\sum{}'' = Kv^2 \tag{2}$$

where, K is the configuration scaling number of the parafoil which is empirically selected between 0.001 and 0.1.

After the conditions for the speed, the drag area and their derivates are provided, the equations (1) and (2) are numerically solved, and the time cost t_f from partial inflation to full deployment is obtained:

$$t_f = 2.93(W/(\rho K g^{0.652}))^{0.377} v_0^{-1.262} \tag{3}$$

where, g is the constant of gravity, and v_0 is the initial speed.

Equation (3) is defined in imperial units. It is tested that the initial vertical speed v_0 has a major effect on the deployment time t_f, and there is a better result utilizing large K under the condition of low speed. After the aircraft falls freely for 1.5 s to obtain an initial vertical speed of 14.7 m/s (48.22 fps) without consideration of fuselage drag, the parafoil deployment time is about 1.71 s with the condition of $K = 0.1$.

B. DYNAMICS MODELING OF THE CANOPY

The external forces acting on the subparts p_i include the aerodynamic force $\boldsymbol{F}_a^{p_i}$, the suspension line tension $\boldsymbol{F}_s^{p_i}$, the connection inner force $\boldsymbol{F}_t^{p_i}$, and the gravity $\boldsymbol{F}_g^{p_i}$. The state variables include the speed vector $\boldsymbol{V}_b^{p_i} = (u^{p_i}, v^{p_i}, w^{p_i})^T$ and the angle rate $\boldsymbol{\omega}^{p_i} = (p^{p_i}, q^{p_i}, r^{p_i})^T$ in the body coordinate system. Based on Newton's second law and the momentum theorem, the kinetic equations for the part p_i are given in the moving coordinate system:

$$\begin{aligned}\dot{\boldsymbol{V}}_b^{p_i} &= (\boldsymbol{m}^{p_i} + \boldsymbol{m}_f^{p_i})^{-1}(\boldsymbol{F}_a^{p_i} + \boldsymbol{F}_s^{p_i} + \boldsymbol{F}_t^{p_i} + \boldsymbol{F}_g^{p_i}) \\ &\quad - \boldsymbol{\omega}^{p_i} \times \boldsymbol{V}_b^{p_i} \end{aligned} \tag{4}$$

$$\dot{\boldsymbol{h}}^{p_i} = \boldsymbol{M}_a^{p_i} + \boldsymbol{M}_s^{p_i} + \boldsymbol{M}_t^{p_i} - \boldsymbol{\omega}^{p_i} \times \boldsymbol{h}^{p_i} \tag{5}$$

where, $\boldsymbol{M}_a^{p_i}$ is the aerodynamic moment. $\boldsymbol{M}_s^{p_i}$ and $\boldsymbol{M}_t^{p_i}$ represent the moments produced by the line tension $\boldsymbol{F}_s^{p_i}$ and the connection force $\boldsymbol{F}_t^{p_i}$, respectively. $\boldsymbol{m}^{p_i}$ and $\boldsymbol{m}_f^{p_i}$ are the mass and the apparent mass matrices. The momentum moment $\boldsymbol{h}^{p_i}$ is expressed as:

$$\boldsymbol{h}^{p_i} = (\boldsymbol{I}^{p_i} + \boldsymbol{I}_f^{p_i})\boldsymbol{\omega}^{p_i} \tag{6}$$

The apparent mass matrices $\boldsymbol{m}_f^{p_i}$ and the inertia matrices $\boldsymbol{I}_f^{p_i}$ induced by the included air mass are estimated through the method provided by Barrows [36], and the time derivative of apparent mass during deployment is ignored.

The control force on each subpart is only related to the trailing-edge deflection of its side, and the roll and yaw moments applied to the canopy are induced by differences in lift and drag between the two sides. The trailing-edge deflection u_i $(i = 1, 2)$ on the left and right parts is obtained as follows using the symmetric and asymmetric control input (δ_s, δ_a):

$$\begin{bmatrix} u_1 \\ u_2 \end{bmatrix} = \begin{bmatrix} \delta_s - \delta_a \\ \delta_s + \delta_a \end{bmatrix} \tag{7}$$

The functions of trailing-edge deflection u_i and local attack angle α^{p_i} are used to define the lift, drag, and pitch moment coefficients for each part:

$$\begin{aligned} C_L^{p_i}(\alpha^{p_i}, u_i) &= \tilde{C}_L^{p_i}(\alpha^{p_i}) + C_{Lu_i}^{p_i} u_i \\ C_D^{p_i}(\alpha^{p_i}, u_i) &= \tilde{C}_D^{p_i}(\alpha^{p_i}) + C_{Du_i}^{p_i} u_i \\ C_M^{p_i}(\alpha^{p_i}, u_i) &= \tilde{C}_M^{p_i}(\alpha^{p_i}) + C_{Mu_i}^{p_i} u_i \end{aligned} \tag{8}$$

where the derivatives $\tilde{C}_L^{p_i}$, $\tilde{C}_D^{p_i}$, $\tilde{C}_M^{p_i}$ to the attack angle and $C_{Lu_i}^{p_i}$, $C_{Du_i}^{p_i}$, $C_{Mu_i}^{p_i}$ to the trailing-edge deflection are obtained through the fitting method based on the data resulting from computational fluid dynamics analysis.

The expanded aerodynamic coefficients along three axes in the body coordinate system are given as [3]:

$$\begin{aligned} C_x^{p_i} &= -(C_D^{p_i} u^{p_i} + C_L^{p_i} w^{p_i})/V^{p_i} \\ C_y^{p_i} &= C_{y\beta}\beta^{p_i} + C_{yr} r^{p_i} b^{p_i}/(2V^{p_i}) \\ C_z^{p_i} &= -(C_D^{p_i} w^{p_i} - C_L^{p_i} u^{p_i})/V^{p_i} \\ C_l^{p_i} &= C_{l\beta}\beta^{p_i} + (C_{lp} p^{p_i} b^{p_i} + C_{lr} r^{p_i} b^{p_i})/(2V^{p_i}) \\ C_m^{p_i} &= C_M^{p_i} + C_{mq} q^{p_i} c/(2V^{p_i}) \\ C_n^{p_i} &= C_{n\beta}\beta^{p_i} + (C_{n\beta} p^{p_i} b^{p_i} + C_{nr} r^{p_i} b^{p_i})/(2V^{p_i}) \end{aligned} \tag{9}$$

where, β^{p_i} is the local sideslip angle, and V^{p_i} is the airspeed. Considering that derivatives $\{C_{y\beta}, C_{yr}, C_{l\beta}, C_{lp}, C_{lr}, C_{mq}, C_{n\beta}, C_{np}, C_{nr}\}$ are approximately independent of the trailing-edge deflection, the superscript p_i is removed.

Finally, the aerodynamic forces and the moments are calculated by:

$$\boldsymbol{F}_a^{p_i} = \frac{1}{2}\rho(V^{p_i})^2 S^{p_i} \begin{bmatrix} C_x^{p_i} \\ C_y^{p_i} \\ C_z^{p_i} \end{bmatrix} \tag{10}$$

$$\boldsymbol{M}_a^{p_i} = \frac{1}{2}\rho(V^{p_i})^2 S^{p_i} \begin{bmatrix} b^{p_i} C_l^{p_i} \\ c C_m^{p_i} \\ b^{p_i} C_n^{p_i} \end{bmatrix} \tag{11}$$

where S^{p_i} denotes the area of the part p_i.

It is assumed that there is linear deformation in the tensile range, and the inner tensions connecting canopy parts are concentrated at the adjacent corner points. The connection force $\boldsymbol{F}_{t_k}^{p_i}$ acting on a corner $\boldsymbol{r}_k^{p_i}$ $(k = 1, \ldots, N_t)$ of the part p_i is related to the position of another part p_j, which is calculated based on their relative stretching deformation. If the stretching deformation is negative, the tension will be nonexistent

without the support of the included air. To identify surface overlapping, the distances from $\boldsymbol{r}_k^{p_i}$ and $\boldsymbol{r}_k^{p_j}$ to the mass center of the part p_i are compared. Therefore, the connection force is expressed as:

$$\boldsymbol{F}_{t_k}^{p_i} = \begin{cases} K_t(\boldsymbol{r}_k^{p_i} - \boldsymbol{r}_k^{p_j}), & ||\boldsymbol{r}_k^{p_i} - \boldsymbol{r}_O^{p_i}|| \le ||\boldsymbol{r}_k^{p_j} - \boldsymbol{r}_O^{p_i}|| \\ \boldsymbol{0}, & ||\boldsymbol{r}_k^{p_i} - \boldsymbol{r}_O^{p_i}|| > ||\boldsymbol{r}_k^{p_j} - \boldsymbol{r}_O^{p_i}|| \end{cases} \tag{12}$$

where, K_t is the elastic coefficient of the canopy, $\boldsymbol{r}_O^{p_i}$ is the position vector of the reference center O^{p_i} of the part p_i in the inertial system. The moment $\boldsymbol{M}_{t_k}^{p_i}$ produced by $\boldsymbol{F}_{t_k}^{p_i}$ is calculated by:

$$\boldsymbol{M}_{t_k}^{p_i} = (\boldsymbol{r}_k^{p_i} - \boldsymbol{r}_O^{p_i}) \times \boldsymbol{F}_{t_k}^{p_i} \tag{13}$$

Thus, the resultant connection tension $\boldsymbol{F}_t^{p_i}$ and moment $\boldsymbol{M}_t^{p_i}$ are obtained respectively as follows:

$$\boldsymbol{F}_t^{p_i} = \sum_{k=1}^{N_t} \boldsymbol{D}_{be}^{p_i} \boldsymbol{F}_{t_k}^{p_i} \tag{14}$$

$$\boldsymbol{M}_t^{p_i} = \sum_{k=1}^{N_t} \boldsymbol{D}_{be}^{p_i} \boldsymbol{M}_{t_k}^{p_i} \tag{15}$$

where, $\boldsymbol{D}_{be}^{p_i}$ is the transformation matrix of the part p_i from the ground coordinate system to the body coordinate system, and it can be calculated by:

$$\boldsymbol{D}_{be} = \begin{bmatrix} c\theta c\psi & c\theta s\psi & -s\theta \\ s\phi s\theta c\psi - c\phi s\psi & s\phi s\theta s\psi + c\phi c\psi & s\phi c\theta \\ c\phi s\theta c\psi + s\phi s\psi & c\phi s\theta s\psi - s\phi c\psi & c\phi c\theta \end{bmatrix} \tag{16}$$

where, ϕ, θ, and ψ are the roll, pitch, and yaw angles, respectively, $s(\cdot)$ is the abbreviation for $\sin(\cdot)$, and $c(\cdot)$ is the abbreviation for $\cos(\cdot)$.

The suspension lines connecting the canopy and the aircraft are assumed to be multi-massless spring systems. The nature length L_n $(n = 1, \ldots, N_s)$ without stretching for each suspension line is designed in advance so that these lines determine the outline of the deployed parafoil. If the mount position of a suspension line on the aircraft is expressed as $\boldsymbol{r}_n^a$, the distance to the mount position $\boldsymbol{r}_n^{p_i}$ (if any) on the corresponding canopy part can be computed. The line tension is then obtained by:

$$\boldsymbol{F}_{s_n}^{p_i} = \begin{cases} K_s(\boldsymbol{r}_n^a - \boldsymbol{r}_n^{p_i}), & \left\|\boldsymbol{r}_n^a - \boldsymbol{r}_n^{p_i}\right\| \ge L_n \\ \boldsymbol{0}, & \left\|\boldsymbol{r}_n^a - \boldsymbol{r}_n^{p_i}\right\| < L_n \end{cases} \tag{17}$$

where K_s is the stiffness of suspension lines. The moment $\boldsymbol{M}_{s_n}^{p_i}$ produced by $\boldsymbol{F}_{s_n}^{p_i}$ is calculated by:

$$\boldsymbol{M}_{s_n}^{p_i} = (\boldsymbol{r}_n^a - \boldsymbol{r}_n^{p_i}) \times \boldsymbol{F}_{s_n}^{p_i} \tag{18}$$

Thus, the resultant line tension $\boldsymbol{F}_s^{p_i}$ and moment $\boldsymbol{M}_s^{p_i}$ are expressed as:

$$\boldsymbol{F}_s^{p_i} = \sum_{n=1}^{N_s} \boldsymbol{D}_{be}^{p_i} \boldsymbol{F}_{s_n}^{p_i} \tag{19}$$

$$\boldsymbol{M}_s^{p_i} = \sum_{n=1}^{N_s} \boldsymbol{D}_{be}^{p_i} \boldsymbol{M}_{s_n}^{p_i} \tag{20}$$

C. DYNAMICS MODELING OF THE VEHICLE

The vehicle is viewed as a 6 DOF rigid body with an invariable center of gravity. The speed $\boldsymbol{V}_b^a = (u^a,\ v^a,\ w^a)^T$ and the angle rate $\boldsymbol{\omega}^a = (p^a,\ q^a,\ r^a)^T$ in the body coordinate system are selected as state variables. The kinetic equations are similar to equations (4) and (5):

$$\dot{\boldsymbol{V}}_b^a = (\boldsymbol{F}_a^a + \boldsymbol{F}_s^a + \boldsymbol{F}_g^a)/m^a - \boldsymbol{\omega}^a \times \boldsymbol{V}_b^a \tag{21}$$

$$\dot{\boldsymbol{h}}^a = \boldsymbol{M}_a^a + \boldsymbol{M}_s^a - \boldsymbol{\omega}^a \times \boldsymbol{h}^a \tag{22}$$

In the above equations, m^a is the vehicle mass. the aerodynamic force $\boldsymbol{F}_a^a$, suspension line tension $\boldsymbol{F}_s^a$, and gravity $\boldsymbol{F}_g^a$ all contribute to the external forces on the aircraft. The external moments involve the aerodynamic moment $\boldsymbol{M}_a^a$ and the moment $\boldsymbol{M}_s^a$ produced by $\boldsymbol{F}_s^a$. The computation for the aerodynamic force $\boldsymbol{F}_a^a$ and moment $\boldsymbol{M}_a^a$ refers to the rotorcraft model provided by Robert Mahony [37]. The mass of the suspension line is unconsidered, thus the line tension $\boldsymbol{F}_s^a$ acting on the aircraft is opposite to the tension $\boldsymbol{F}_s^{p_i}$ on the canopy. The calculation of the moment $\boldsymbol{M}_s^a$ is similar to the procedure in (18) and (20).

III. COMPARATIVE ANALYSIS OF THE DYNAMICS MODEL

To verify the flexible model built in the paper, the basic flight performance is compared with the results from other modeling methods. Moreover, a flight experiment is carried out to provide further verification.

A. COMPARISON BETWEEN DIFFERENT METHODS

The simulation result from a 9 DOF model referring to Ref. [3] is compared with the flexible model, including straight gliding and turning flight, and a simple 6 DOF rigid model is used as a comparison. These models adopt the same parafoil geometry and aerodynamic lift and drag characteristics to maintain consistency, in which the span is 7.5 m, the chord is 3.75 m, the parafoil mass is 5 kg and the payload is 135 kg.

The straight glide trajectories under the varied symmetric trailing-edge deflection δ_s are presented in Fig. 4(a). It is found that the flexible model has a similar response to the longitudinal control input with the 9 DOF model. The glide ratio for three models in steady status are both near the value of 2.86 without control input. The 9 DOF model has a lower glide ratio of about 0.76 when the full deflection command $\delta_s = 100\%$ is given, and the corresponding value for the flexible model is 1.03.

The turning flight is tested under the asymmetric deflection of $\delta_a = 50\%$, and the horizontal and vertical motion trajectories are provided in Fig. 5. There is a good coherence of turning performance that the flight radiuses are 67 m, 77 m, and 72 m for the 9 DOF, 6 DOF and the flexible models, respectively. It also is noticed that a displacement derivation appears between the horizontal trajectories of the flexible model and the 9 DOF model induced by the difference of response speed to the control input. The result of vertical motions in Fig. 5(b) indicates that the glide ratio during the

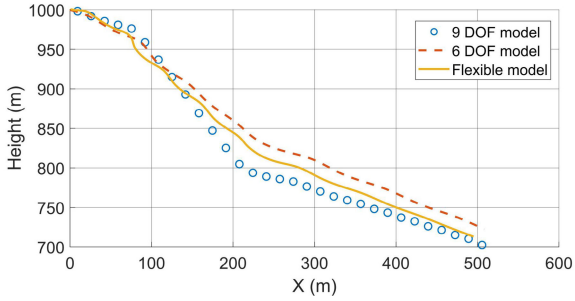

(a) Glide trajectories of different dynamics models

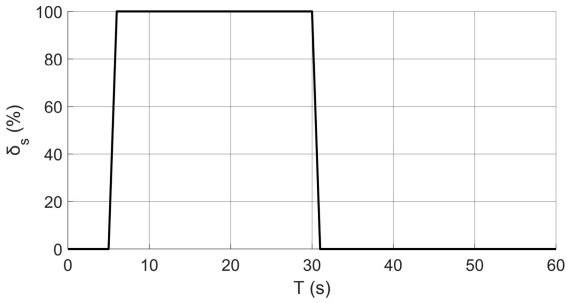

(b) The symmetric trailing

FIGURE 4. The comparison between different models for straight glide.

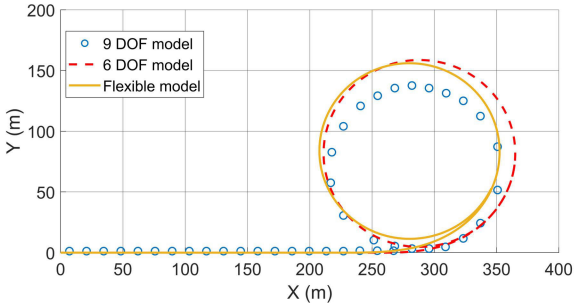

(a) Horizontal trajectory

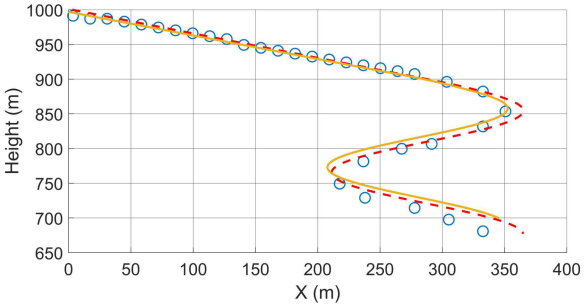

(b) Vertical trajectory

FIGURE 5. The turning flight trajectories under the asymmetric trailing-edge deflection $\delta_a = 50\%$.

turning circle is reduced compared with the straight glide, and the glide ratio of the flexible model is reduced to 2.44.

B. FLIGHT PERFORMANCE EXPERIMENT

A powered parafoil system is built as shown in Fig. 6 to make a comparison with the mathematical model. The parafoil span is 4.1 m, and the chord is 1.6 m. There are two motors in front and back of the payload respectively to provide thrusts and offset rotor torques, and two actuators on lateral sides to control trailing-edge deflections. This system can take off in a short distance using its own lift and thrust without additional facilities.

The flight experiment under remote control was conducted to measure actual flight data. During the flight, the parafoil climbs up using thrusts, and the power system will be closed to begin a glide when the parafoil reaches a certain height. The flight trajectory and the height change are shown in Fig. 7. There are two phases of unpowered glide operated. In glide phase 1 of Fig. 7(b), the longitudinal control input is 100% between 487 s and 522 s and the glide ratio observed is about 2.38. From 522 s to 1252 s, the flight height is raised again and the direction is adjusted to prepare for the next glide. In phase 2 between 1252 s and 1309 s, the longitudinal control input is 50% and the glide ratio observed is about 3.03. Because the glide ratio is less effected by the payload weight that the increase of weight primarily makes glide faster, the obtained result for glide ratio can be as the reference value for the system with different payloads.

Using the same parafoil parameters, the straight glide of the flexible model is tested, and the glide trajectories under different inputs are given in Fig. 8. The glide ratio is (3.64, 2.99, 2.54) responding to the longitudinal input (0, 50%, 100%), which is relatively consistent with the experimental data.

IV. TRAJECTORY OPTIMIZATION WITH MULTIPLE OBJECTIVES

While the parafoil is deployed, a reference trajectory from the current position to the landing target is calculated for guidance.

Because the motion range of unpowered glide is determined by the glide performance of the parafoil, the pseudo-spectral method [38] is used to generate a reference trajectory satisfying flight dynamics.

A. PLANNING METHOD BASED ON THE OPTIMAL CONTROL PROBLEM

Considered that the mission requirement is to avoid existing obstacles while using the least amount of energy possible. Based on the optimization control problem, the objective function can be presented in Bolza form [39]:

$$\min\ J = f_1 \left\| \boldsymbol{r}(t_f) - \tilde{\boldsymbol{r}}_{t_f} \right\| + f_2 \int_{t_0}^{t_f} |\delta_a|^2 \, dt \tag{23}$$

$$\text{s.t.} \begin{cases} \dot{\boldsymbol{X}} = \boldsymbol{f}(\boldsymbol{X},\ \boldsymbol{U},\ t) \\ \boldsymbol{X}_{\max} \geq \boldsymbol{X} \geq \boldsymbol{X}_{\min} \\ \boldsymbol{U}_{\max} \geq \boldsymbol{U} \geq \boldsymbol{U}_{\min} \\ C(x,\ y,\ z) > 0 \end{cases} \tag{24}$$

where, $\tilde{r}_{tf}$ is the expected landing position, f_i $(i = 1, 2)$ is the coefficient to adjust the weight for the optimization objectives

(a) The powered parafoil system

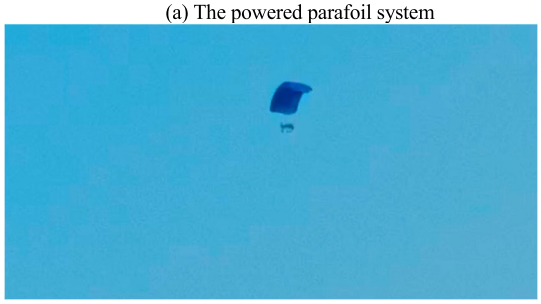

(b) Flying using rotor thrusts

FIGURE 6. The outside view and flight process of the powered parafoil system.

landing precision and minimal energy consumption, and $C(x, y, z)$ is a function of the current position in the path constraint. The control input $\boldsymbol{U}$ denotes the asymmetric and symmetric trailing-edge deflection $(\delta_a,\ \delta_s)^T$, and the integral over δ_a in the right second item of equation (23) represents the energy consumption used to control flight. Because the states of the parafoil and the vehicle are different, the system generally is treated as a rigid system in trajectory planning, and the system state $\boldsymbol{X}$ is taken as the state which related to the gravity center of the whole system, including the speed $\boldsymbol{V}_b = (u,\ v,\ w)^T$, the angle rate $\boldsymbol{\omega} = (p,\ q,\ r)^T$, the attitude angle $\boldsymbol{\Theta} = (\phi,\ \theta,\ \psi)^T$, and the position $\boldsymbol{r} = (x,\ y,\ z)^T$.

Considering that spatial motions and directional changes are the main concerns instead of pitching and rolling motions in trajectory planning, a 4-DOF model is adopted to improve computational efficiency [40]. The longitudinal and lateral attitude motions are neglected, and the translational and directional motions are remained to keep the primary glide and turn performances. The simplified model is written as follows:

$$\begin{cases} \dot{x} = V_{xy}\cos\psi + \Delta V_x \\ \dot{y} = V_{xy}\sin\psi + \Delta V_y \\ \dot{\psi} = \bar{U} \\ \dot{z} = V_z \end{cases} \tag{25}$$

where, V_{xy} is the horizontal component of the speed, V_z is the vertical component, and $(\Delta V_x,\ \Delta V_y)$ represents external wind efforts. V_{xy} and V_z generally are constant and determine a reference glide ratio k_{cont}. There is a corresponding relationship between the yaw angle rate $\dot{\psi}$ and the asymmetric trailing-edge deflection δ_a, the directional control $\bar{U}$ equal to $\dot{\psi}$ is defined and employed to simplify the expression.

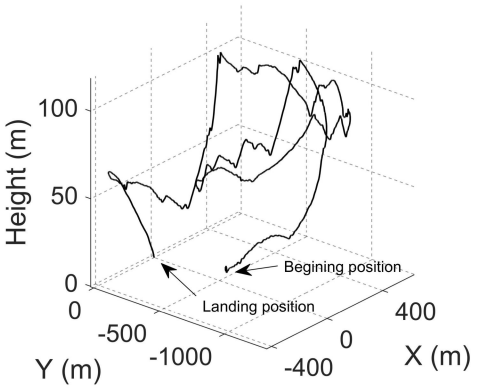

(a) Three-dimension flight trajectory

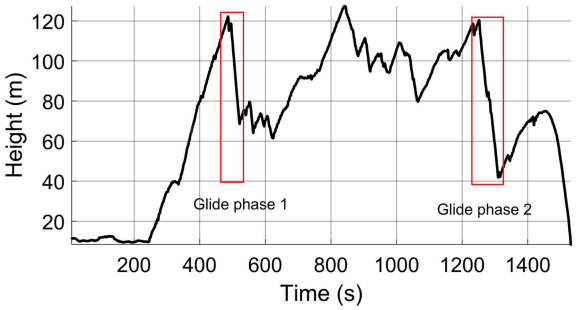

(b) Height-time curve of the flight

FIGURE 7. Motion trajectory and height change of the flight experiment.

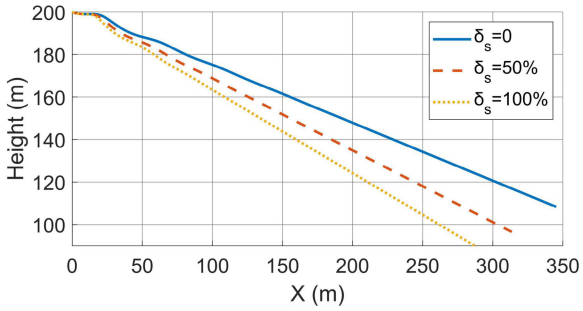

FIGURE 8. Glide trajectories of the flexible model under different longitudinal inputs.

The avoid collisions between the parafoil and the obstacle, the planned trajectory should always be upon the obstacle. Hence, $C(x,\ y,\ z)$ in (24) used for the path constraint is designed as:

$$C(x,\ y,\ z) = -(z - P(x,\ y)) \tag{26}$$

where $P(x, y)$ representing the altitude is a function of horizontal coordinates.

B. DISCRETIZATION OF THE TRAJECTORY OPTIMIZATION PROBLEM

The optimization problem defined by (23) and (24) needs to be converted into a discrete nonlinear programming problem (NLP) to solve [41].

According to the two-point boundary value problem, the required time $t_0 \in [t_0,\ t_f]$ taken for landing is first scaled to $\tau \in [-1,\ 1]$, and the mapping relationship is expressed as:

$$\tau = \frac{2}{t_f - t_0}(t - \frac{t_f + t_0}{2}) \tag{27}$$

where, τ_k $(k = 1, \ldots, N)$ denotes the Legendre Gauss (LG) collocation point, which is the root of the Nth-order Legendre polynomial. The point $\tau_0 = -1$ corresponding to the beginning time t_0 is added to this time set additionally.

The system state and the control input are estimated respectively using Lagrange interpolation as follows:

$$\boldsymbol{X}(\tau) = \sum_{i=0}^{N} L_i(\tau)\boldsymbol{X}(\tau_i) \tag{28}$$

$$\boldsymbol{U}(\tau) = \sum_{i=1}^{N} \tilde{L}_i(\tau)\boldsymbol{U}(\tau_i) \tag{29}$$

where, $L_i(\tau)$ and $\tilde{L}_i(\tau)$ $(i \neq 0)$ are the Nth-order and the $(N\text{-}1)$th-order Lagrange polynomials:

$$L_i(\tau) = \prod_{j=0, j\neq i}^{N} \frac{\tau - \tau_j}{\tau_i - \tau_j} \tag{30}$$

$$\tilde{L}_i(\tau) = \prod_{j=1, j\neq i}^{N} \frac{\tau - \tau_j}{\tau_i - \tau_j} \tag{31}$$

Thus, dynamic constraints in the point τ_k can be expressed as:

$$\dot{\boldsymbol{X}}(\tau_k) = \sum_{i=0}^{N} \dot{L}_i(\tau_k)\boldsymbol{X}(\tau_i) \tag{32}$$

The final state at the endpoint $\tau_{N+1} = -1$ is estimated through the Gauss integral formula:

$$\boldsymbol{X}(\tau_f) = \boldsymbol{X}(\tau_0) + \frac{t_f - t_0}{2}\sum_{k=1}^{N} \omega_k \boldsymbol{f}(\boldsymbol{X}(\tau_k), \boldsymbol{U}(\tau_k), \tau_k) \tag{33}$$

where ω_k is Gauss integral coefficient.

Through the above process, the discrete form of the continuous optimization problem is obtained:

$$\min\ J = f_1 \left\| \boldsymbol{r}(\tau_f) - \tilde{\boldsymbol{r}}_{t_f} \right\| + f_2 \frac{t_f - t_0}{2} \sum_{k=1}^{N} \omega_k \left|\delta_a(\tau_k)\right|^2 \tag{34}$$

$$\text{s.t.} \begin{cases} \sum_{i=0}^{N} \dot{L}_i(\tau_k)\boldsymbol{X}_i - \frac{t_f - t_0}{2}\boldsymbol{f}(\boldsymbol{X}(\tau_k), \boldsymbol{U}(\tau_k), \tau_k) = \boldsymbol{0} \\ \boldsymbol{X}_{\max} \geq \boldsymbol{X}(\tau_k) \geq \boldsymbol{X}_{\min} \\ \boldsymbol{U}_{\max} \geq \boldsymbol{U}(\tau_k) \geq \boldsymbol{U}_{\min} \\ C(\boldsymbol{x}(\tau_k), \boldsymbol{y}(\tau_k), \boldsymbol{z}(\tau_k)) > 0 \end{cases} \tag{35}$$

Using the solver based on the sequential quadratic programming method, the discrete optimization problem in (34) and (35) is solved to generate a series of waypoints for guidance.

V. TRAJECTORY FOLLOWING OF THE PARAFOIL SYSTEM

A four-channel proportional-integral controller is used to control the aircraft attitude and height during the powered flight. The autonomous system will turn off the aircraft control and switch to parafoil control once the parafoil is deployed. Because the parafoil plays a major role in aerodynamic effects during the unpowered glide, the parafoil states are selected as the controlled variables.

To track the waypoints $\{P(1), P(2), \ldots, P(N)\}$ generated by trajectory planning, the dual-channel control scheme is designed as shown in Fig. 9, in which the subscript *mea* represents the measured state and the subscript *ref* represents the reference command. Yaw angle rate and yaw angle controls are accomplished in the directional control one after the other. The yaw angle rate $\dot{\psi}$ is approximately replaced by the angle rate r along the z-axis of the body coordinate system. There is a nonlinear relationship between pitch attitude and turn maneuver that the pitch angle also would increase as increasing the asymmetric deflection during a turning flight. Thus, the glide ratio k is directly controlled instead of the pitch angle in the longitudinal control. The actual glide ratio is estimated by dividing the forward speed by the descending speed, and a second-order low-pass filter is used to eliminate glitches.

A. ALLOCATION METHOD FOR THE CONTROL OUTPUTS

The directional and the longitudinal controls both are implemented through trailing-edge deflections (δ_a, δ_s). As the symmetrical deflection δ_s changes from zero to its maximum value, the glide ratio is gradually decreased. However, the glide ratio also will be influenced by the input of the asymmetric deflection. To reduce this coupling effect, the allocation strategy between the two channels is first considered.

The signal of the trailing-edge deflection (u_L, u_R) for each side is normalized to [0, 1] from the physical dimension. The control signal should be the sum of outputs of the two-channel controller, in which δ_s generated by the longitudinal control varies between 0 and 1, and δ_a generated by the directional control varies between -0.5 and 0.5. As illustrated in Fig. 10, to maintain the same asymmetric deflection, the part that exceeds the movable range is offset by adjusting the other side deflection. The control outputs are distributed in the way described below to the bilateral deflections for the left and right canopy parts:

$$(u_L,\ u_R) = \begin{cases} (c_1,\ c_2) & 1 \geq c_1 \geq 0,\ 1 \geq c_2 \geq 0 \\ (1,\ 1 + c_2 - c_1) & c_1 > 1,\ 1 \geq c_2 \geq 0 \\ (0,\ c_2 - c_1) & 0 > c_1,\ 1 \geq c_2 \geq 0 \\ (1 + c_1 - c_2,\ 1) & 1 \geq c_1 \geq 0,\ c_2 > 1 \\ (c_1 - c_2,\ 0) & 1 \geq c_1 \geq 0, 0 > c_2 \end{cases} \tag{36}$$

where, $c_1 = \delta_s - \delta_a$ and $c_2 = \delta_s + \delta_a$ are defined as the initial unregulated signals.

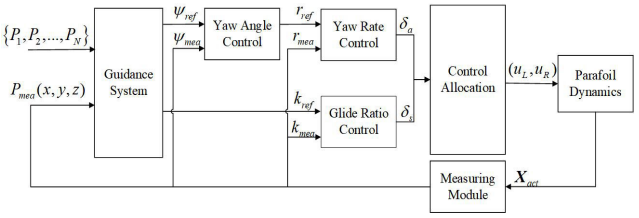

FIGURE 9. The dual-channel flight control diagram of the parafoil system.

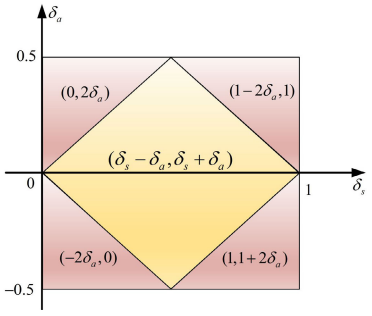

FIGURE 10. The distribution diagram of left and right deflections (u_L, u_R) corresponding to control signals.

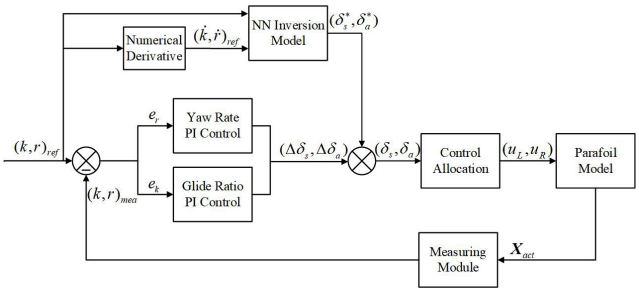

FIGURE 11. The diagram for the inner loop control adopting neural network prediction.

B. DESIGN OF THE DIRECTIONAL AND GLIDING CONTROLS

As shown in Fig. 11, the inner-loop control is designed with incremental form that the base input (δ_a^*, δ_s^*) is approximated through a neural network inversion model, and the incremental input ($\Delta\delta_a$, $\Delta\ \delta_s$) is generated through proportional-integral control.

The inversion model based on the feed-forward neural network is used to reduce the control coupling. As shown in Fig. 12, the neural network is composed of n_i input neurons, one hidden layer with n_j neurons, and n_k output neurons. $\boldsymbol{X}^1$ represents the network input, $\boldsymbol{X}^2$ represents the output in the hidden layer, and $\boldsymbol{Y}$ represents the network output. The output in each layer is calculated by:

$$\boldsymbol{X}^2 = \boldsymbol{f}(\hat{\boldsymbol{X}}^2) = \boldsymbol{f}(\boldsymbol{W}^1\boldsymbol{X}^1 + \boldsymbol{B}^1) \tag{37}$$

$$\boldsymbol{Y} = \boldsymbol{W}^2\boldsymbol{X}^2 + \boldsymbol{B}^2 \tag{38}$$

where, $\boldsymbol{W}^1$ and $\boldsymbol{B}^1$ are weight and bias respectively between the input and the hidden layers. $\boldsymbol{W}^2$ and $\boldsymbol{B}^2$ are weight and bias between the hidden and the output layers. The activation function $f(\cdot)$ is a logistic function as follows:

$$f(x) = \frac{1}{1+e^{-x}} \tag{39}$$

Especially, its derivative is expressed as:

$$f'(x) = f(x)(1-f(x)) \tag{40}$$

The model is trained by the sample data resulting from different work conditions. For sample points $\{(\tilde{\boldsymbol{X}}^1, \tilde{\boldsymbol{Y}})_1, \cdots, (\tilde{\boldsymbol{X}}^1, \tilde{\boldsymbol{Y}})_p, \cdots, (\tilde{\boldsymbol{X}}^1, \tilde{\boldsymbol{Y}})_{n_p}\}$, the total loss function is defined by:

$$E = \sum_{p=1}^{n_p} E_p = \sum_{p=1}^{n_p}\sum_{k=1}^{n_3} \frac{1}{2}(Y_{pk} - \tilde{Y}_{pk})^2 \tag{41}$$

Based on the gradient descent method, the updated weight and bias in the iteration step q are updated for the next iteration step $(q+1)$ as follows:

$$\boldsymbol{W}_{q+1} = \boldsymbol{W}_q - \eta_W(\frac{\partial E}{\partial \boldsymbol{W}})_q \tag{42}$$

$$\boldsymbol{B}_{q+1} = \boldsymbol{B}_q - \eta_B(\frac{\partial E}{\partial \boldsymbol{B}})_q \tag{43}$$

where, η_W and η_B are the learning rates of weight and bias, respectively. The partial derivatives of the loss function respect to the weight element W_{kj}^2 and W_{ji}^1 are calculated by:

$$\frac{\partial E}{\partial W_{kj}^2} = \frac{1}{2}\sum_{p=1}^{n_p}\frac{\partial(Y_{pk} - \tilde{Y}_{pk})^2}{\partial W_{kj}^2} = \sum_{p=1}^{n_p}(Y_{pk} - \tilde{Y}_{pk})X_j^2 \tag{44}$$

$$\begin{aligned}\frac{\partial E}{\partial W_{ji}^1} &= \frac{1}{2}\sum_{p=1}^{n_p}\frac{\partial\sum_{k=1}^{n_2}(Y_{pk} - \tilde{Y}_{pk})^2}{\partial W_{ji}^1} \\ &= \sum_{p=1}^{n_p}\sum_{k=1}^{n_3}(Y_{pk} - \tilde{Y}_{pk})\frac{\partial Y_{pk}}{\partial X_j^2}\frac{\partial X_j^2}{\partial \hat{X}_j^2}\frac{\partial \hat{X}_j^2}{\partial W_{ji}^1} \\ &= \sum_{p=1}^{n_p}\sum_{k=1}^{n_3}(Y_{pk} - \tilde{Y}_{pk})W_{kj}^2 X_j^2(1-X_j^2)X_i^1\end{aligned} \tag{45}$$

The partial derivatives of the loss function respect to the weight elements B_k^2 and B_j^1 are calculated by:

$$\frac{\partial E}{\partial B_k^2} = \frac{1}{2}\sum_{p=1}^{n_p}\frac{\partial(Y_{pk} - \tilde{Y}_{pk})^2}{\partial B_k^2} = \sum_{p=1}^{n_p}(Y_{pk} - \tilde{Y}_{pk}) \tag{46}$$

$$\begin{aligned}\frac{\partial E}{\partial B_j^1} &= \frac{1}{2}\sum_{p=1}^{n_p}\frac{\partial\sum_{k=1}^{n_3}(Y_{pk} - \tilde{Y}_{pk})^2}{\partial B_j^1} \\ &= \sum_{p=1}^{n_p}\sum_{k=1}^{n_3}(Y_{pk} - \tilde{Y}_{pk})\frac{\partial Y_{pk}}{\partial X_j^2}\frac{\partial X_j^2}{\partial \hat{X}_j^2}\frac{\partial \hat{X}_j^2}{\partial B_j^1} \\ &= \sum_{p=1}^{n_p}\sum_{k=1}^{n_3}(Y_{pk} - \tilde{Y}_{pk})W_{kj}^2 X_j^2(1-X_j^2)\end{aligned} \tag{47}$$

The dynamic changes of expected states are included in the inversion model, thus the control input (δ_a^*, δ_s^*) is estimated

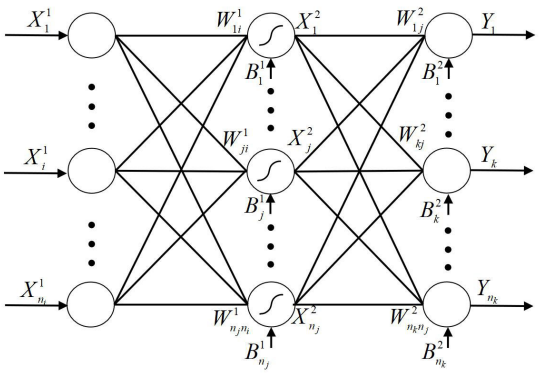

FIGURE 12. The neural network diagram with a hidden layer.

as follows:

$$\begin{bmatrix} \delta_s^* \\ \delta_a^* \end{bmatrix} = \boldsymbol{W}^2 \boldsymbol{f}(\boldsymbol{W}^1 \begin{bmatrix} k_{ref} \\ \dot{k}_{ref} \\ r_{ref} \\ \dot{r}_{ref} \end{bmatrix} + \boldsymbol{B}^1) + \boldsymbol{B}^2 \tag{48}$$

The incremental inputs are added up to improve control effectiveness especially in the initial phase and expressed as:

$$\Delta\delta_s = K_{Ps}(k_{ref} - k_{mea}) + K_{Is}\int (k_{ref} - k_{mea})dt \tag{49}$$

$$\Delta\delta_a = K_{Pa}(r_{ref} - r_{mea}) + K_{Ia}\int (r_{ref} - r_{mea})dt \tag{50}$$

where, K_{Ps}, K_{Is}, K_{Pa}, and K_{Ia} are gain coefficients, k_{ref} is the expected glide ratio. The expected angle rate r_{ref} is produced through the outer-loop control:

$$r_{ref} = K_{Pr}(\psi_{ref} - \psi_{mea}) + K_{Ir}\int (\psi_{ref} - \psi_{mea})dt \tag{51}$$

where, K_{Pr} and K_{Ir} are gain coefficients, ψ_{ref} is the expected yaw angle.

Thus, the control signals for symmetric and asymmetric deflections are obtained:

$$\begin{bmatrix} \delta_s \\ \delta_a \end{bmatrix} = \begin{bmatrix} \delta_s^* \\ \delta_a^* \end{bmatrix} + \begin{bmatrix} \Delta\delta_s \\ \Delta\delta_a \end{bmatrix} \tag{52}$$

C. GUIDANCE COMMANDS GENERATED FROM WAYPOINTS

The method of sight guidance is used to produce reference states k_{ref} and ψ_{ref} for the parafoil controller through the discrete waypoints [40]. When the parafoil is flying between two waypoints $P(i)$ and $P(i+1)$, the base glide ratio is first obtained by:

$$k_{base} = \frac{\sqrt{(P_x(i+1) - P_x(i))^2 + (P_y(i+1) - P_y(i))^2}}{P_z(i+1) - P_z(i)} \tag{53}$$

Because the velocity observed exists in an oscillating state, the actual sight line is defined by relative position instead of the velocity vector. The glide slope of pointing to $P(i+1)$ from the measured current position $P_{mea}(x, y, z)$ is expressed as:

$$k_{poi} = \frac{\sqrt{(P_x(i+1) - x)^2 + (P_y(i+1) - y)^2}}{P_z(i+1) - z} \tag{54}$$

Thus, the increment of approaching the base glide line is calculated by:

$$\Delta k = \frac{k_{poi} - k_{base}}{\eta_g} \tag{55}$$

where η_g is the coefficient to adjust convergence speed. Finally, the reference glide ratio provided for the longitudinal controller is given as:

$$k_{ref} = k_{base} + \Delta k \tag{56}$$

where the desired glide ratio k_{ref} is limited to the interval [2.4, 3.6] corresponding to the allowable range.

Similarly to the above procedure, the expected yaw angle is calculated on the horizontal plane as follows:

$$\psi_{ref} = \psi_{base} + \Delta\psi \tag{57}$$

where the base yaw angle and the increment are given respectively by:

$$\psi_{base} = \arctan(\frac{P_y(i+1) - P_y(i)}{P_x(i+1) - P_x(i)}) \tag{58}$$

$$\Delta\psi = (\arctan(\frac{P_y(i+1) - y}{P_x(i+1) - x}) - \psi_{base})/\eta_p \tag{59}$$

where η_p is the convergence factor.

TABLE 1. Parameter setting of the parafoil-vehicle system.

Symbol	Parameter	Value
c	Canopy chord	2.83 m
b^{p_i}	Spans of canopy subparts	3.79 m
m^p	Canopy mass	3 kg
m^a	Vehicle mass	90 kg
L_1,	Lengths of front suspension lines	4.955 m
L_2	Lengths of rear suspension lines	5.704 m
L_c	Length of leading-edge cut	0.1415 m
l	Distance between connection point and canopy top	7.217 m
γ	Half angle between outside lines	30 degrees

VI. SIMULATIONS AND ANALYSES

Simulations are carried out to verify the parafoil-vehicle system with trajectory planning and following. Table 1 lists the values of primary parameters used in the dynamics model. There are different conditions designed in simulations, including autonomous landing, wind resistance, and obstacle avoidance.

A. AUTONOMOUS LANDING

In the simulation, three flight phases are designed to test the landing precision of the autonomous control system. At the beginning, the quadrotor located at $P_0 = (-330\text{ m}, 100\text{ m}, -210\text{ m})$ speeds up to 5 m/s with a yaw angle of 0 deg under flight control. Then, the parafoil is released at $t_p = 10$ s and begins to deploy. Finally, the parafoil reaches a steady status and glides to the target along the reference trajectory.

In trajectory planning, the optimization objectives of landing precision and minimal energy consumption are considered, of which the weight coefficients are taken as $\{f_1, f_2\} = \{0.5, 0.5\}$ in the optimal function (23), the range of control input related to the turn rate is $|\bar{U}| \leq 0.09$, and the reference constant glide ratio is set as $k_{cont} = 3$. Because it takes some time before the guidance and control come into play, the beginning point of the planned trajectory is at $(-300\text{ m}, 100\text{ m}, -200\text{ m})$.

Fig. 13(a) depicts the three-dimensional motions of the canopy parts and the aircraft in the inertial coordinate system in the simulation. The results show that the system can better achieve a precise landing and the aircraft lands on the ground with a position error of about 6.6 m. Because the simplified dynamics model is adopted in the planning procedure, computation time is less than one second.

Fig. 14 presents the time curves of flight states in the simulation, including the speed (V_x, V_y, V_z) in the geodetic coordinate system, the attitude angle (ϕ, θ, ψ), and the position (x, y, z) in the geodetic coordinate system. The results indicate that the states vary dramatically during the transition, and it takes about 4 s to fully reach a new steady status, in which the lost altitude is about 16 m. As shown in Fig. 14(d), the aircraft initially rolls to the right and then stabilizes with a roll angle close to zero. The canopy experiences a transient impact that causes a pitch angle of about 14 deg, and the pendulum motion appears momentarily due to the stabilizing effect of the aircraft gravity.

It is found that the yaw angle of the aircraft also changes rapidly during the transition. Due to control errors, the flight direction of the aircraft is not exactly ideal along the expected straight line. There is a sideslip angle for the aircraft and a relative yaw angle between the aircraft and the canopy before the transition phase. As a result, unbalanced line tensions are produced and induces the interaction effect between the rolling movement of the aircraft and the asymmetric behavior for parts p_1 and p_2. Moreover, the asymmetric trailing-edge deflection actuated by flight control also has a contribution to the phenomena. As shown in Fig. 14(f), the maximum relative yaw angle of 25 deg between the aircraft and the canopy is gradually corrected during the straight glide flight, and the turning flight can increase this relative angle.

The canopy initially is folded so that its right and left parts have roll angles of nearly 90 degrees with opposite signs. The steady roll angle for each part is approximately equal to the value of 49 degrees with opposite signs. The canopy parts are not completely constrained and they are relatively rotatable to each other. Thus, the steady status of the canopy

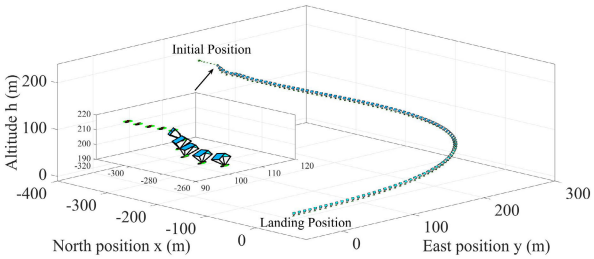

FIGURE 13. Three-dimensional flight trajectory of the parafoil-vehicle system including powered flight and unpowered glide.

is influenced by its lift characteristics and the weight of the aircraft.

Fig. 15 gives the response curves for yaw motions and glide ratio variations under parafoil control. It can be found that the rapid changes of glide ratio and yaw rate appears when the parafoil is being deployed, and the states both tend to follow the expected value later. Because the reference trajectory consists of discrete waypoints, it can be clear to find the zigzag responses of the yaw rate caused by the sequential change of waypoints. The expected glide ratio is always around the reference value $k_{cont} = 3$ in trajectory planning, and the position error related to the reference trajectory is corrected by changing the glide ratio by a small amount.

B. WIND RESISTANCE

In view of the fact that the parafoil is sensitive to wind disturbance, the simulations under different conditions of external winds are conducted to analyze the wind resistance of the autonomous landing system. There are the same initial configurations of the system as in subsection VI.A. It is assumed that the global wind field applied during the parafoil glide flight is constant and horizontal, and its flow direction angle is 45 deg in the ground coordinate system. Because the flight speed of the parafoil is around 6 m/s, the range of the wind speed ΔV is given as from 0 to 3 m/s.

Fig. 16 gives the flight trajectories under conditions of different wind speeds. It is found that the designed direction control is proven to resist the external wind. The landing errors are listed in Table 2. The results show that the landing precision is influenced by the magnitude of wind speed. Under the condition of wind speed $\Delta V = 3$ m/s, the transient glide ratio could be reduced to a minimum of around 1.4 when the parafoil is at some specific inflow directions concerning the wind. The mean glide ratio generally is reduced as increasing the wind speed throughout the flight, the parafoil would land ahead of the expected target even with input saturation.

Because the adjustment range of the glide slope is limited by the reduction of glide performance in the wind fields, the reference glide ratio k_{cont} in trajectory optimization is changed from 3.0 to 2.9, and the simulations are conducted with the same conditions as above. Fig. 17 gives the corresponding flight trajectories in simulations. The flight distance is a bit reduced compared with the results in Fig. 16,

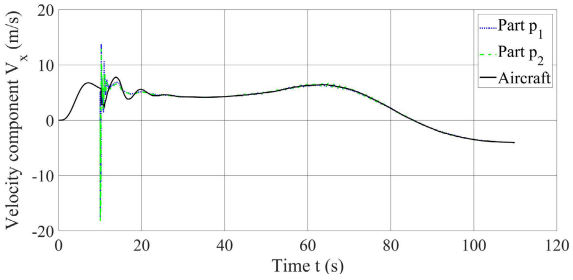

(a) North component of velocity

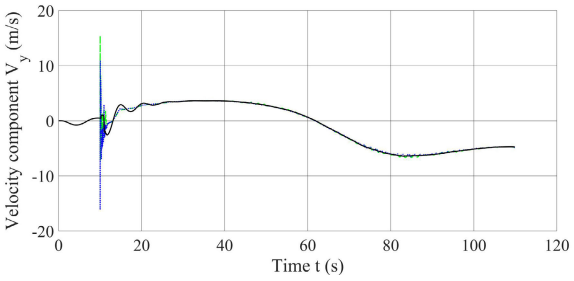

(b) East component of velocity

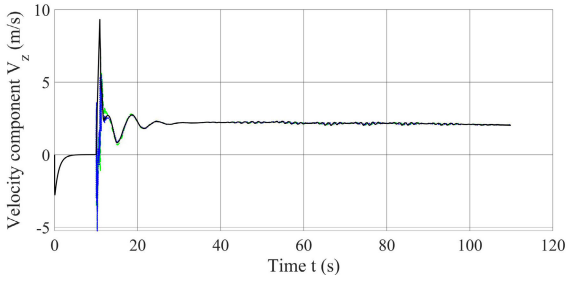

(c) Vertical component of velocity

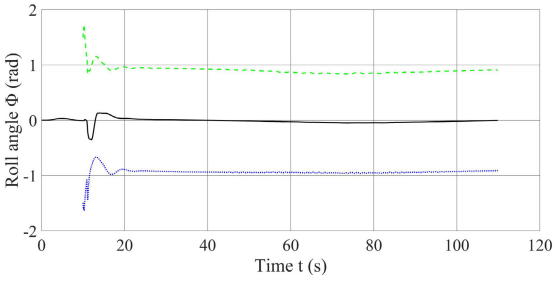

(d) Roll angle

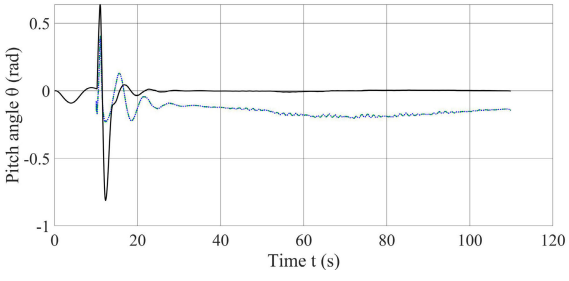

(e) Pitch angle

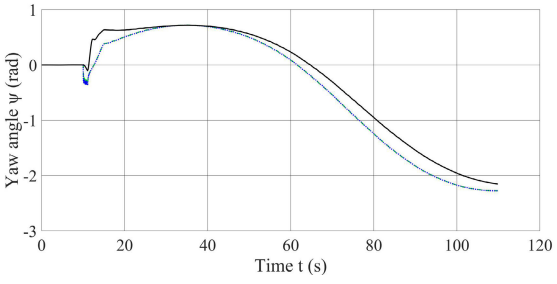

(f) Yaw angle

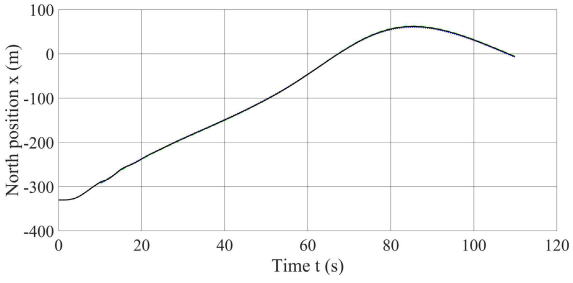

(g) North position

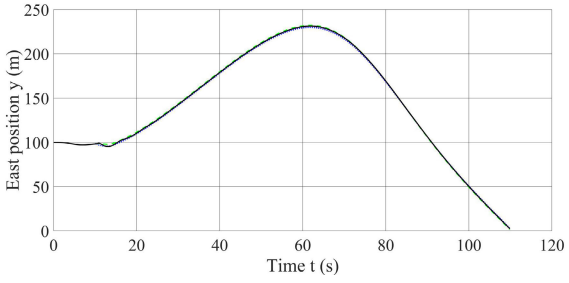

(h) East position

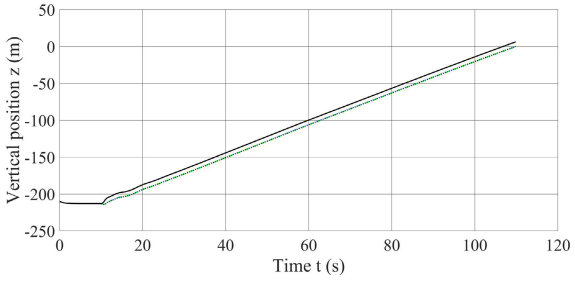

(i) Vertical position

FIGURE 14. The time curves of the linear and attitude motions for the aircraft and canopy subparts, in which the black solid line denotes the aircraft, the blue dotted line denotes the right canopy part, and the green dashed line denotes the left canopy part.

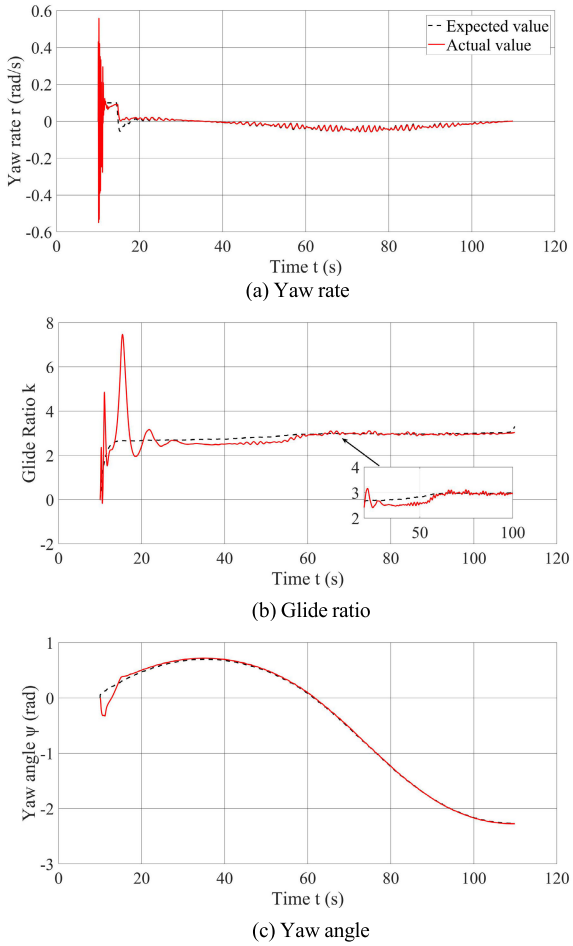

FIGURE 15. Response curves of directional and gliding controls.

TABLE 2. Landing errors along the reference trajectory in wind fields.

Wind speed ΔV	3 m/s	2 m/s	1 m/s	0
Landing position (x, y)	(25.5 m, 40.3 m)	(10.9 m, 28.3 m)	(5.3 m, 13.2 m)	(-6.1 m, 2.5 m)

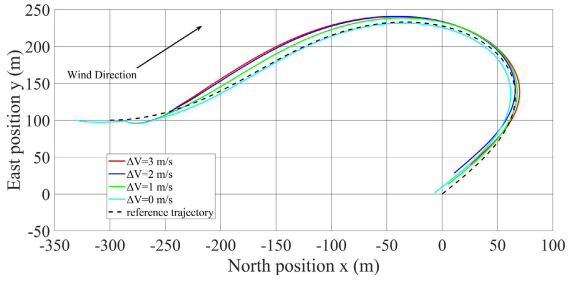

FIGURE 16. Horizontal flight trajectories of simulations under different wind speeds compared with reference trajectory.

and the parafoil also can track the reference trajectory well in different wind fields. The landing positions are listed in

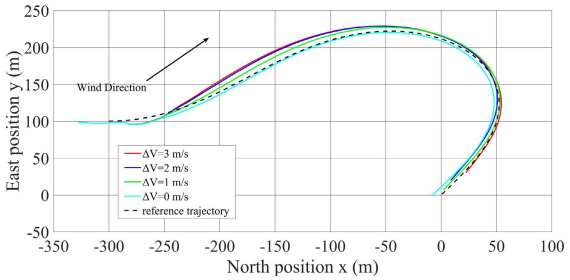

FIGURE 17. Horizontal flight trajectories of simulations under different wind speeds when the reference glide ratio is equal to 2.9.

TABLE 3. Landing errors when reducing reference glide ratio in wind fields.

Wind speed ΔV	3 m/s	2 m/s	1 m/s	0
Landing position (x, y)	(22.4 m, 30.3 m)	(8.7 m, 19.9 m)	(2.1 m, 7.0 m)	(-7.9 m, -0.2 m)

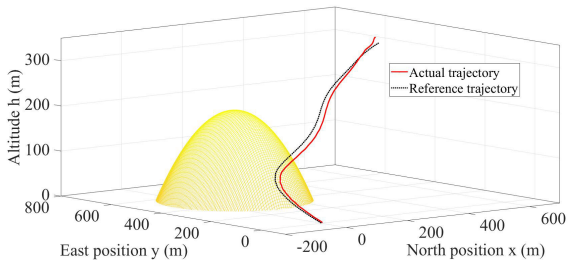

FIGURE 18. Flight trajectory and planned path to avoid an obstacle, in which the black scatter line represents the planned path and the red line represents the actual flight trajectory.

Table 3. The landing errors generally are reduced compared with the results in Table 2 except without wind disturbance. It is indicated that the landing error induced by the reduction of glide performance can be compensated through trajectory planning to some extent, and an appropriately reduced k_{cont} is beneficial to improve the landing precision of the parafoil in wind fields.

C. OBSTACLE AVOIDANCE

The obstacle is introduced into the simulation to verify the ability of obstacle avoidance. The aircraft is initially set at $P_0 = (660\text{ m}, 540\text{ m}, -310\text{ m})$ with a yaw angle of 180 deg. Besides landing precision and energy consumption, the obstacle is designed in trajectory planning. The obstacle altitude $P(x, y)$ in the path constraint (26) is represented as a paraboloid function:

$$P(x,\ y) = -h_t + ((x - x_t)^2 + (y - y_t)^2)/d \qquad (60)$$

where, the obstacle center (x_t, y_t) is (92 m, 461 m), the altitude h_t is equal to 200 m, and the parameter d related to the altitude-width ratio is 200.

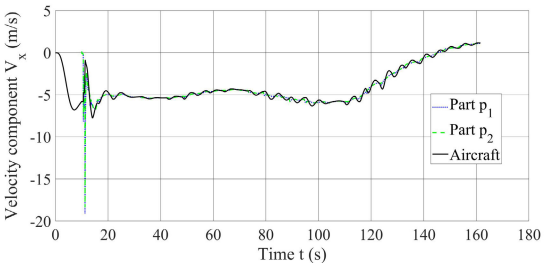

(a) North component of velocity

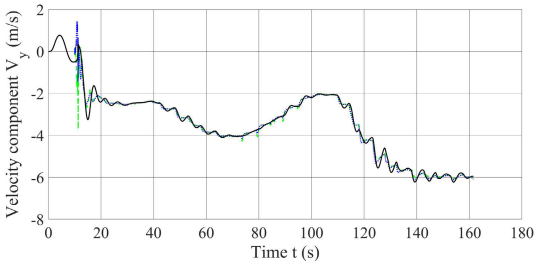

(b) East component of velocity

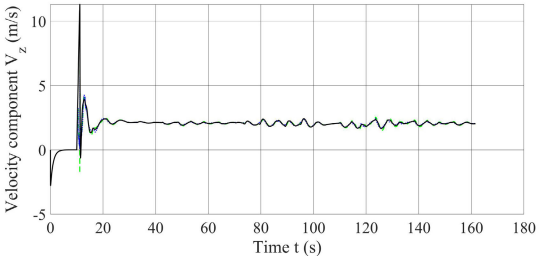

(c) Vertical component of velocity

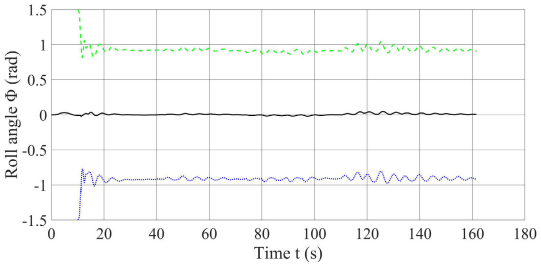

(d) Roll angle

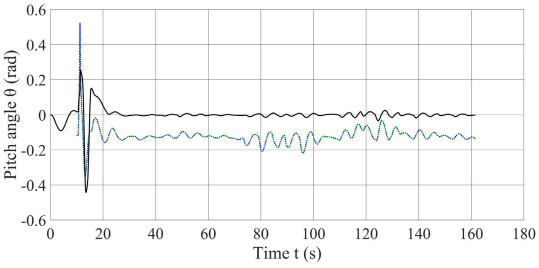

(e) Pitch angle

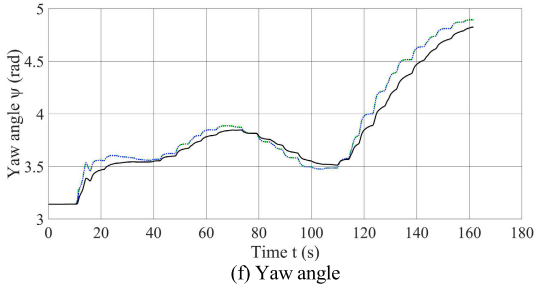

(f) Yaw angle

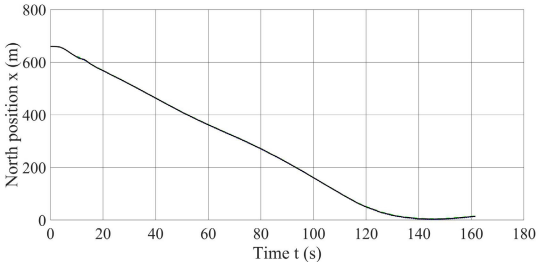

(g) North position

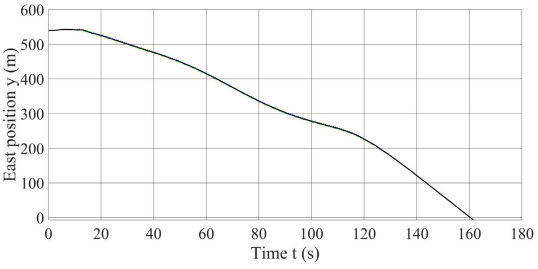

(h) East position

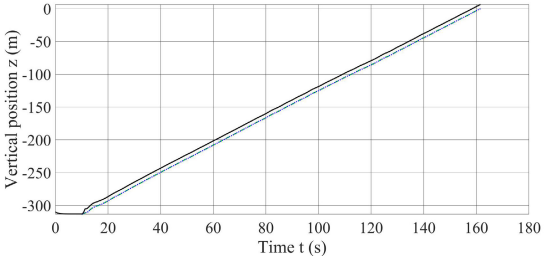

(i) Vertical position

FIGURE 19. **The time curves of the linear and attitude motions in the flight of avoiding an obstacle.**

Due to aircraft movements, it is challenging to guarantee that the starting positions of the planned trajectory and the actual glide flight coincide completely. A distance advance is given and the initial position deviation is corrected by

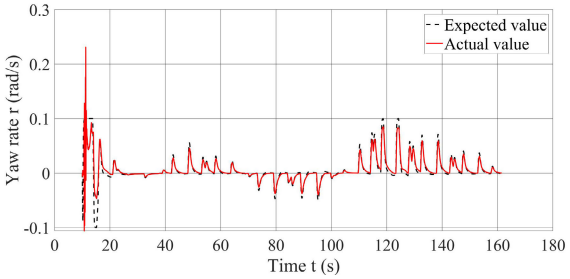

(a) Yaw rate

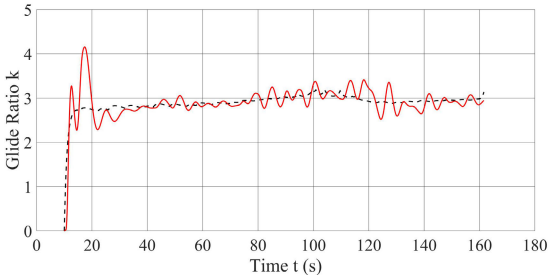

(b) Glide ratio

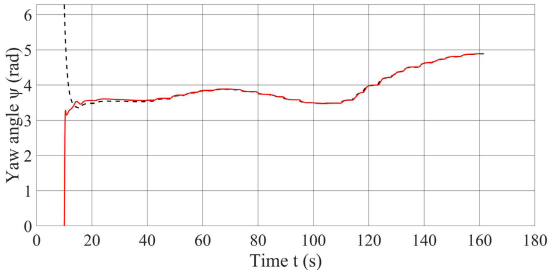

(c) Yaw angle

FIGURE 20. Response curves of directional and gliding controls in the flight of avoiding an obstacle.

guiding the parafoil into the reference trajectory. Fig. 18 depicts the motion trajectory in simulation and reference trajectory. The results indicate that the parafoil system can track the planned trajectory well and the final landing error is about 10 m. The time cost to generate a guidance trajectory is less than 2 s, which is acceptable in the real-time simulation environment.

The rapid state changes in the transition also appear as shown in the response curves of system states of Fig. 19. Following the deployment of the parafoil, the roll angles of the right and left parts stabilize at close to 50 deg with opposite signs. And the pitch angles both are around −8 degrees, which is comparable to the results without an obstruction. Despite the downward glide trajectory, the attack angle is still positive and the lift is produced. In contrast to the earlier results, the aircraft enters the reference trajectory without much roll motions that the line tensions are nearly symmetrically distributed during the deployment process. The relative yaw angle between the aircraft and canopy still rises when the parafoil enters a turn. The designed twist spring connection is expected to provide directional restoring moments for the aircraft, and its following performance is not required strictly because of the large movable range for a practical hook-loop structure.

The response curves for yaw attitude and glide ratio are shown in Fig. 20. The number of waypoints is reduced from 100 to 40 to speed up computation, and the expected state changes significantly between two adjacent waypoints. When the guidance waypoint is switched to the next, the yaw rate variation becomes more evident. It is also discovered that the time scale of the longitudinal channel is longer than the directional channel, and more time is needed to follow the expected glide ratio.

VII. CONCLUSION

In the paper, the coupled parafoil-vehicle dynamics model is built as the basis of control and guidance designs, in which the system framework involving powered flight and unpowered glide is developed. To account for flexible deformations occurring during the deployment process, the canopy is designed as comprising symmetric right and left parts. The pseudo-spectral method is employed to generate a reference trajectory of satisfying system dynamics, and multiple optimization objectives are considered for different instances. The directional and gliding control is designed by combining the proportional integral control with the neural network inversion model. For the saturation of the trailing-edge deflections, the output signals are regulated to reduce coupling between the two control channels. The autonomous landing system is validated through simulations under various conditions. The conclusion is drawn from the results:

1) The detailed variation of the coupled system during the airdrop process is obtained through the designed model. It is found that, during the transition from aircraft flight to parafoil glide, the aircraft gravity produces a stabilizing effect resulting in a temporary pendulum motion of the system. The lost altitude required to reach a steady glide is obtained. When the initial forward speed of the aircraft is 5 m/s, the lost altitude is about 16 m. The states of the left and right canopy subparts are not the same in the refined model, and unbalanced line tensions and aerodynamic forces on the two sides could induce asymmetric rolling movements. Compared with traditional multibody models, there is more unsteady motion information obtained to analyze through the flexible model.
2) Multiple optimization objectives are achieved in trajectory planning. The parafoil can follow the reference trajectory well using the designed controller, and the landing errors are less than 10 m in ideal circumstances. In wind fields, the system still has a strong ability to control flight direction. Due to the degradation of glide performance caused by the wind, the parafoil will land ahead of the target position if the reference trajectory is calculated according to the situation without external disturbances. The land accuracy is improved under the wind condition after the reference glide ratio is reduced

appropriately. The autonomous motion problem for the parafoil is dealt well through the combination of flight control and trajectory planning.

The works in the paper complement the research of the multibody parafoil dynamics and trajectory following. The designed integrated autonomous landing system can apply to different vehicles equipped with a parafoil, and is beneficial for the research of parafoil recovery technology. The flight experiment for the real-time trajectory planning and autonomous control will be carried out in future works.

REFERENCES

[1] F. Lv, W. He, and L. Zhao, "An improved nonlinear multibody dynamic model for a parafoil-UAV system," *IEEE Access*, vol. 7, pp. 139994–140009, 2019.

[2] Y. Ochi, "Modeling and simulation of flight dynamics of a relative-roll-type parafoil," in *Proc. AIAA Scitech Forum*, Jan. 2020, p. 1643.

[3] O. Prakash and N. Ananthkrishnan, "Modeling and simulation of 9-DOF parafoil-payload system flight dynamics," in *Proc. AIAA Atmos. Flight Mech. Conf. Exhib.*, Aug. 2006, p. 6130.

[4] H. Yang, L. Song, and W. Chen, "Research on parafoil stability using a rapid estimate model," *Chin. J. Aeronaut.*, vol. 30, no. 5, pp. 1670–1680, Oct. 2017.

[5] W. Wu, Q. Sun, M. Sun, M. Dehmer, and Z. Chen, "Modeling and control of parafoils based on computational fluid dynamics," *Appl. Math. Model.*, vol. 70, pp. 378–401, Jun. 2019.

[6] H. Zhu, Q. Sun, X. Liu, J. Liu, H. Sun, W. Wu, P. Tan, and Z. Chen, "Fluid–structure interaction-based aerodynamic modeling for flight dynamics simulation of parafoil system," *Nonlinear Dyn.*, vol. 104, no. 4, pp. 3445–3466, Jun. 2021.

[7] H. Zhu, Q. Sun, J. Tao, Z. Chen, M. Dehmer, and G. Xie, "Flexible modeling of parafoil delivery system in wind environments," *Commun. Nonlinear Sci. Numer. Simul.*, vol. 108, May 2022, Art. no. 106210.

[8] M. Ward, M. Costello, and N. Slegers, "Specialized system identification for parafoil and payload systems," *J. Guid., Control, Dyn.*, vol. 35, no. 2, pp. 588–597, Mar. 2012.

[9] X. Wang, J. Liu, X. Su, H. Peng, X. Zhao, and C. Lu, "A review on carrier aircraft dispatch path planning and control on deck," *Chin. J. Aeronaut.*, vol. 33, no. 12, pp. 3039–3057, Dec. 2020.

[10] B. Le Floch, J. How, L. Breger, and M. Stoeckle, "Trajectory planning for autonomous parafoils in complex terrain," in *Proc. 24th AIAA Aerodynamic Decelerator Syst. Technol. Conf.*, Jun. 2017, p. 3220.

[11] B. Luders, A. Ellertson, J. P. How, and I. Sugel, "Wind uncertainty modeling and robust trajectory planning for autonomous parafoils," *J. Guid., Control, Dyn.*, vol. 39, no. 7, pp. 1614–1630, Jul. 2016.

[12] H. Sun, S. Luo, Q. Sun, Z. Chen, W. Wu, and J. Tao, "Trajectory optimization for parafoil delivery system considering complicated dynamic constraints in high-order model," *Aerosp. Sci. Technol.*, vol. 98, Mar. 2020, Art. no. 105631.

[13] Z. Zhang, Z. Zhao, and Y. Fu, "Dynamics analysis and simulation of six DOF parafoil system," *Cluster Comput.*, vol. 22, no. S5, pp. 12669–12680, Sep. 2019.

[14] A. V. S. Babu, V. C. Suja, and C. V. Reddy, "Three dimensional trajectory optimization of a homing parafoil," *IFAC Proc. Volumes*, vol. 47, no. 1, pp. 847–854, 2014.

[15] B. J. Rademacher, P. Lu, A. L. Strahan, and C. J. Cerimele, "In-flight trajectory planning and guidance for autonomous parafoils," *J. Guid., Control, Dyn.*, vol. 32, no. 6, pp. 1697–1712, Nov. 2009.

[16] L. Fowler and J. Rogers, "Bézier curve path planning for parafoil terminal guidance," *J. Aerosp. Inf. Syst.*, vol. 11, no. 5, pp. 300–315, May 2014.

[17] N. Slegers and C. Gorman, "Comparison and analysis of multi-body parafoil models with varying degrees of freedom," in *Proc. 21st AIAA Aerodynamic Decelerator Syst. Technol. Conf. Seminar*, May 2011, p. 2615.

[18] J. Rogers and N. Slegers, "Robust parafoil terminal guidance using massively parallel processing," *J. Guid., Control, Dyn.*, vol. 36, no. 5, pp. 1336–1345, Sep. 2013.

[19] O. Prakash and N. Anathkrishnan, "NDI based generic heading tracking control law for parafoil/payload system," in *Proc. AIAA Aviation Forum*, Jun. 2020, p. 3195.

[20] Y. Li, M. Zhao, M. Yao, Q. Chen, R. Guo, T. Sun, T. Jiang, and Z. Zhao, "6-DOF modeling and 3D trajectory tracking control of a powered parafoil system," *IEEE Access*, vol. 8, pp. 151087–151105, 2020.

[21] P. Tan, Q. Sun, Z. Chen, and Y. Jiang, "Characteristic model–based generalized predictive control and its application to the parafoil and payload system," *Optim. Control Appl. Methods*, vol. 40, no. 4, pp. 659–675, Jul. 2019.

[22] N. Slegers and M. Costello, "Model predictive control of a parafoil and payload system," *J. Guid., Control, Dyn.*, vol. 28, no. 4, pp. 816–821, Jul. 2005.

[23] W. Gockel and W. Gockel, "Concept studies of an autonomous GNC system for gliding parachute," in *Proc. 14th Aerodynamic Decelerator Syst. Technol. Conf.*, Jun. 1997, p. 1465.

[24] S. He, S.-L. Dai, Z. Zhao, and T. Zou, "Uncertainty and disturbance estimator-based distributed synchronization control for multiple marine surface vehicles with prescribed performance," *Ocean Eng.*, vol. 261, Oct. 2022, Art. no. 111867.

[25] H. Sun, Q. Sun, M. Sun, J. Tao, and Z. Chen, "Accurate modeling and homing control for parafoil delivery system based on wind disturbance rejection," *IEEE Trans. Aerosp. Electron. Syst.*, vol. 58, no. 4, pp. 2916–2934, Aug. 2022.

[26] M. Ward and M. Costello, "Adaptive glide slope control for parafoil and payload aircraft," *J. Guid., Control, Dyn.*, vol. 36, no. 4, pp. 1019–1034, Jul. 2013.

[27] M. Ward, S. Culpepper, and M. Costello, "Parafoil control using payload weight shift," *J. Aircr.*, vol. 51, no. 1, pp. 204–215, Jan. 2014.

[28] E. Scheuermann, M. Ward, M. R. Cacan, and M. Costello, "Combined lateral and longitudinal control of parafoils using upper-surface canopy spoilers," *J. Guid., Control, Dyn.*, vol. 38, no. 11, pp. 2122–2131, Nov. 2015.

[29] A. Gavrilovski, M. Ward, and M. Costello, "Parafoil control authority with upper-surface canopy spoilers," *J. Aircr.*, vol. 49, no. 5, pp. 1391–1397, Sep. 2012.

[30] J. Liu, X. Dong, J. Wang, C. Lu, X. Zhao, and X. Wang, "A novel EPT autonomous motion control framework for an off-axle hitching tractor-trailer system with drawbar," *IEEE Trans. Intell. Vehicles*, vol. 6, no. 2, pp. 376–385, Jun. 2021.

[31] J. Lee and Y. Kim, "Neural network-based nonlinear dynamic inversion control of variable-span morphing aircraft," *Proc. Inst. Mech. Eng., G, J. Aerosp. Eng.*, vol. 234, no. 10, pp. 1624–1637, Aug. 2020.

[32] C. Lv, Y. Xing, J. Zhang, X. Na, Y. Li, T. Liu, D. Cao, and F.-Y. Wang, "Levenberg–Marquardt backpropagation training of multilayer neural networks for state estimation of a safety-critical cyber-physical system," *IEEE Trans. Ind. Informat.*, vol. 14, no. 8, pp. 3436–3446, Aug. 2018.

[33] N. Slegers and M. Costello, "Aspects of control for a parafoil and payload system," *J. Guid., Control, Dyn.*, vol. 26, no. 6, pp. 898–905, Nov. 2003.

[34] M. Nosratollahi and M. A. Ghapanvary, "A novel algorithm for conceptual design and optimisation of an affordable gliding airdrop platform using TCOMOGA," *Aeronaut. J.*, vol. 122, no. 1252, pp. 933–959, Jun. 2018.

[35] J. Potvin, G. Peek, and B. Brocato, "Modeling the inflation of ram-air parachutes reefed with sliders," *J. Aircr.*, vol. 38, no. 5, pp. 818–827, Sep. 2001.

[36] T. M. Barrows, "Apparent mass of parafoils with spanwise camber," *J. Aircr.*, vol. 39, no. 3, pp. 445–451, May 2002.

[37] R. Mahony, V. Kumar, and P. Corke, "Multirotor aerial vehicles: Modeling, estimation, and control of quadrotor," *IEEE Robot. Autom. Mag.*, vol. 19, no. 3, pp. 20–32, Sep. 2012.

[38] L. Yang, W. Chen, X. Liu, and H. Zhou, "Steady glide dynamic modeling and trajectory optimization for high lift-to-drag ratio reentry vehicle," *Int. J. Aerosp. Eng.*, vol. 2016, pp. 1–14, Aug. 2016.

[39] D. A. Benson, "A Gauss pseudospectral transcription for optimal control," Ph.D. dissertation, Dept. Aeronaut. Astronaut., Massachusetts Inst. Technol., Cambridge, MA, USA, 2004.

[40] L. Zhang, H. Gao, Z. Chen, Q. Sun, and X. Zhang, "Multi-objective global optimal parafoil homing trajectory optimization via Gauss pseudospectral method," *Nonlinear Dyn.*, vol. 72, nos. 1–2, pp. 1–8, Apr. 2013.

[41] Q. Chen, X. Wang, and J. Yang, "Optimal path-following guidance with generalized weighting functions based on indirect Gauss pseudospectral method," *Math. Problems Eng.*, vol. 2018, pp. 1–17, Aug. 2018.

[42] N. Murali, M. Dineshkumar, K. W. C. Arun, and D. S. Sheela, "Guidance of parafoil using line of sight and optimal control," *IFAC Proc. Volumes*, vol. 47, no. 1, pp. 870–877, 2014.

LUQI YAN received the B.S. degree in aircraft design and engineering from the Zhengzhou University of Aeronautics, Zhengzhou, in 2017, and the M.S. degree in aircraft design from the Nanjing University of Aeronautics and Astronautics, Nanjing, in 2020, where he is currently pursuing the Ph.D. degree in aircraft design with the College of Aerospace Engineering.

His research interest includes flight simulation and control.

YANGUO SONG received the Ph.D. degree from the Nanjing University of Aeronautics and Astronautics, Nanjing, in 2003.

He is currently an Associate Professor with the Nanjing University of Aeronautics and Astronautics. His research interests include helicopter flight dynamics and control, and helicopter design.

HUANJIN WANG received the Ph.D. degree in aircraft design from the Nanjing University of Aeronautics and Astronautics, Nanjing, in 2002.

She is currently an Associate Professor with the Nanjing University of Aeronautics and Astronautics. Her research interests include helicopter flight dynamics, aerodynamics, and flight control.

ZHIWEI SHI received the Ph.D. degree in fluid mechanics from the Nanjing University of Aeronautics and Astronautics, Nanjing, in 2006.

He is currently a Professor with the Nanjing University of Aeronautics and Astronautics. His research interests include fluid mechanics, and flight dynamics and control.